AGU PUBLICATIONS

JGR

Journal of Geophysical Research: Solid Earth

RESEARCH ARTICLE
10.1002/2017JB014566

Special Section:
Rock Physics of the Upper Crust

**Key Points:**
- We perform numerical upscaling experiments to obtain attenuation and modulus dispersion of seismic waves due to fluid pressure diffusion
- The 2-D stochastic fracture networks, representing natural fracture networks as closely as possible for these studies, are considered
- Sensitivity of fracture-to-background and fracture-to-fracture fluid pressure diffusion to local fracture connectivity is observed

**Correspondence to:**
J. Hunziker,
jurg.hunziker@unil.ch

**Citation:**
Hunziker, J., Favino, M., Caspari, E., Quintal, B., Rubino, J. G., Krause, R., & Holliger, K. (2018). Seismic attenuation and stiffness modulus dispersion in porous rocks containing stochastic fracture networks. *Journal of Geophysical Research: Solid Earth*, *123*, 125–143. https://doi.org/10.1002/2017JB014566

Received 15 JUN 2017
Accepted 30 NOV 2017
Accepted article online 2 JAN 2018
Published online 11 JAN 2018



# Seismic Attenuation and Stiffness Modulus Dispersion in Porous Rocks Containing Stochastic Fracture Networks

**Jürg Hunziker[1], Marco Favino[1,2], Eva Caspari[1], Beatriz Quintal[1], J. Germán Rubino[3], Rolf Krause[2], and Klaus Holliger[1]**

[1] Institute of Earth Sciences, University of Lausanne, Lausanne, Switzerland, [2] Institute of Computational Science, Università della Svizzera italiana, Lugano, Switzerland, [3] CONICET, Centro Atómico Bariloche-CNEA, San Carlos de Bariloche, Argentina

**Abstract** Understanding seismic attenuation and modulus dispersion mechanisms in fractured rocks can result in significant advances for the indirect characterization of such environments. In this paper, we study attenuation and modulus dispersion of seismic waves caused by fluid pressure diffusion (FPD) in stochastic 2-D fracture networks, allowing for a state-of-the-art representation of natural fracture networks by a power law length distribution. To this end, we apply numerical upscaling experiments consisting of compression and shear tests to our samples of fractured rocks. The resulting *P* and *S* wave attenuation and modulus dispersion behavior is analyzed with respect to the density, the length distribution, and the connectivity of the fractures. We focus our analysis on two manifestations of FPD arising in fractured rocks, namely, fracture-to-background FPD at lower frequencies and fracture-to-fracture FPD at higher frequencies. Our results indicate that FPD is sensitive not only to the fracture density but also to the geometrical characteristics of the fracture length distributions. In particular, our study suggests that information about the local connectivity of a fracture network could be retrieved from seismic data. Conversely, information about the global connectivity, which is directly linked to the effective hydraulic conductivity of the probed volume, remains rather difficult to infer.

## 1. Introduction

The characterization of fractured formations, notably with regard to their hydraulic behavior, is essential for a wide range of practically important applications, such as, for example, geothermal energy production, hydrocarbon exploration, nuclear waste disposal, or $CO_2$ storage. Relating measured seismic attributes directly to individual fractures is difficult, since seismic wavelengths are typically much larger than the fracture sizes. However, obtaining information about fractured rocks in an effective medium framework is possible. For such purposes many analytical effective medium models have been developed (e.g., Chapman, 2003, 2009; Gurevich et al., 2009; Liu et al., 2000; Schoenberg & Sayers, 1995). It has been demonstrated that the overall orientation and density of fracture networks below the seismic resolution from such analytical models can be reliably inferred from seismic data (Liu & Martinez, 2012). Conversely, the estimation of characteristics controlling the hydraulic behavior, such as aperture, length distribution, and connectivity of the fractures, remains enigmatic.

Grechka and Kachanov (2006) have shown that in an elastic context, the degree of connectivity of fracture networks has a negligible effect on the seismic response. However, recent poroelastic studies (e.g., Quintal et al., 2014; Rubino et al., 2013, 2014; Vinci et al., 2014) have demonstrated that in the presence of connected fractures, two manifestations for *P* and *S* wave attenuation prevail. One is governed by fluid pressure diffusion (FPD) between the fractures and their embedding background and the other one by FPD within connected fractures. For fracture networks with a constant density of fractures of identical size but different degrees of connectivity, the relative importance of the two manifestations of FPD can be directly related to the degree of connectivity (Rubino et al., 2017). These results are encouraging as they indicate that the degree of fracture connectivity, a key parameter for assessing the corresponding hydraulic behavior, could potentially be retrieved from seismic data. However, these initial studies considered rather simplistic models due to numerical limitations. For more realistic fracture networks, the interrelations between seismic attenuation and fracture connectivity remain as of yet entirely unknown.

Natural environments tend to be characterized by fractures comprising a wide range of sizes and their connectivity strongly depends on the fracture length distribution (e.g., de Dreuzy et al., 2001). Common representations of natural fracture systems are based on power law length distributions (e.g., Bonnet et al., 2001). For this study, we choose three scenarios of power law length distributions, covering the range of typical parameter values, to analyze the attenuation behavior of *P* and *S* waves at various fracture densities. This allows us to systematically explore the sensitivity of attenuation with regard to the length distribution and the number of connections characterizing a fracture network. In order to focus on the impact of the geometrical characteristics of the fracture networks, the individual fractures feature all the same physical properties, which is not necessarily realistic but simplifies the analysis.

Since numerical simulations of wave propagation to study FPD effects in rocks containing stochastic fracture networks are computationally very expensive, we use an upscaling procedure, such as those proposed by Masson and Pride (2007), Rubino et al. (2009), and Quintal et al. (2011). To this end, we simulate numerically oscillatory compression and shear tests. In doing so, we assume that the considered poroelastic fractured medium can be replaced by an equivalent viscoelastic medium (Jänicke et al., 2015; Solazzi et al., 2016), for which we then retrieve the frequency-dependent *P* wave and *S* wave modulus dispersion and attenuation. These numerical upscaling experiments are carried out on representative 2-D samples of fractured formations. The fractures are considered as mesoscopic heterogeneities with scales that are much larger than the pore size but smaller than the seismic wavelength. They are modeled as highly compliant, highly porous, and permeable features embedded in a much stiffer, much less porous, and permeable background medium. The upscaling procedure consists of solving the quasi-static poroelastic equations (Biot, 1941) in the frequency domain with boundary conditions depending on the type of test. With the objective of performing such compression and shear tests on stochastic fracture networks, Hunziker et al. (2017) developed a finite-element code based on the open-source framework MOOSE (http://mooseframework.org).

The paper starts by explaining the considered stochastic fracture model and the numerical upscaling procedure, followed by the presentation of the results of the numerical simulations and their interpretation considering the fluid pressure distribution and the local contribution to the overall seismic attenuation.

## 2. Fracture Model

Natural fracture systems can often be characterized by power law length distributions (e.g., Bonnet et al., 2001). The following stochastic distribution *n* for the fracture length *l* is proposed by de Dreuzy et al. (2001)

$$n(l, L) = d_c L^2 (a-1) \frac{l^{-a}}{l_{\min}^{-a+1}} \text{ for } l \in [l_{\min}, l_{\max}], \tag{1}$$

where *L* denotes the side length of the sample and $l_{\min}$ and $l_{\max}$ the minimum and maximum fracture lengths, respectively. The exponent *a* affects the steepness of the distribution and, correspondingly, the relative probability of longer and shorter fractures. A larger value of *a* produces more shorter fractures than longer ones, while a smaller value of *a* produces a flatter distribution with an increasing probability of larger fractures.

The fracture density $d_c$ is defined by de Dreuzy et al. (2001) as the number of fracture centers per unit area. In our study, we use the fracture density $d_a$ denoting the area covered by fractures per unit area. The redefined fracture density allows to distinguish between the effects of the fracture volume fraction and length distribution on the poroelastic properties, which is not straightforward with the original parameterization. To keep the units unchanged, we drop the factor $L^2$ from equation (1).

While the lengths of our rectangular fractures are drawn from the power law distribution described above, the orientations of the fractures and the positions of the fracture centers are drawn from a uniform distribution. The thickness of all fractures is constant and equal to 0.5 mm. Two fractures are considered as connected if their surface areas exhibit any overlap.

The side length *L* of the sample was fixed at 0.4 m. This value was chosen as a trade-off between maximizing the sample size while still being able to fit the sample into the memory of a normal node of our cluster, even for large fracture densities. The maximum fracture length was set to be $l_{\max} = L/2 = 0.2$ m, because having fractures larger than half the sample size would mechanically weaken the sample tremendously. As the fracture aperture is fixed to 0.5 mm, this fracture length corresponds to an aspect ratio of fracture length to fracture aperture of 400. The minimum length of a fracture is set to $l_{\min} = 0.01$ m, which corresponds to an

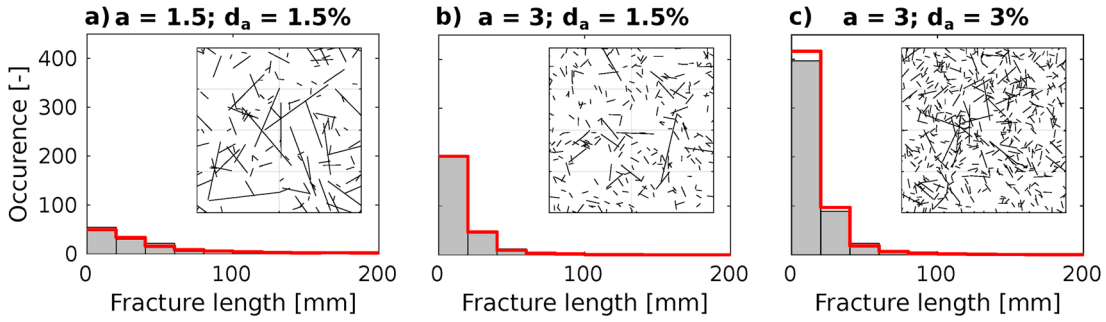


**Figure 1.** Length distributions and the corresponding fracture networks (insets) for three different fracture networks. The mean length distribution, considering the 20 networks drawn for each parameter combination, is shown with a red line. The corresponding values of the characteristic exponent $a$ and the fracture density $d_a$ are given on top of each plot.

aspect ratio of 20. Vermilye and Scholz (1995) report aspect ratios of real fractures between 122 and 666.7. Only on one site, they observed extreme aspect ratios larger than 1,000. Renshaw and Park (1997) found aspect ratios which are as low as 40. Thus, our parameterization is consistent with the range of aspect ratios found in natural rocks.

We vary the fracture density $d_a$ from 1.5% to 3.25% and consider three characteristic exponents of the fracture size distribution: $a = 1.5$, $a = 2.25$, and $a = 3$. For each parameter combination, we generate 20 stochastic fracture networks. To illustrate the diversity of the considered stochastic fracture networks, we show three examples in Figure 1. For each example, the length distribution and the network itself are plotted. Increasing the parameter $a$ increases the amount of shorter fractures at the expense of the longer ones (comparison of Figures 1a and 1b). By increasing the fracture density $d_a$, the relative probability with regard to fracture length is not changed, but the number of fractures in the sample is increased (comparison of Figures 1b and 1c).

The range of considered exponents $a$ comprises end-member scenarios of fracture connectivity with respect to power law length distributions (e.g., Bour and Davy, 1997; de Dreuzy et al., 2001). For 2-D networks with $a > 3$, short fractures determine the connectivity of the system (i.e., an occasional long fracture would not alter the connectivity at the given scale) and classical percolation theory applies. Conversely, for systems with $a < 2$, connectivity is determined by long fractures and the contribution of small fractures is negligible. These latter types of networks approach the connectivity behavior of a set of infinite fractures (de Dreuzy et al., 2001). Consequently, the fracture networks for $a < 2$ contain sample-spanning permeable paths, so-called backbones, at much lower fracture densities than networks associated with higher values of $a$. The number of fracture networks with $a = 1.5$ that have a horizontal, a vertical or both types of backbones is listed in Table 1 for the considered fracture densities $d_a$. No fracture network with $a = 2.25$ or $a = 3$ features a backbone at the considered fracture densities. As we are interested in obtaining information about the hydraulic conductivity of our samples through the study of seismic attenuation, we will discuss the effect of these backbones on the attenuation in the results section.

## 3. Numerical Upscaling Procedure

To find the attenuation and modulus dispersion of an equivalent viscoelastic medium for the considered fractured poroelastic sample, we perform compressibility and shear tests (Rubino et al., 2009). To this end,

**Table 1**
*Number of Fracture Networks of the 20 Realizations Generated for Each Parameter Combination Having a Horizontal, a Vertical, or Both Types of Backbones for a = 1.5*

| $d_a$ (%) | Horizontal backbone | Vertical backbone | Horizontal and vertical backbones |
|---|---|---|---|
| 1.5 | 1 | 0 | 0 |
| 2.25 | 1 | 0 | 0 |
| 2.75 | 7 | 6 | 3 |
| 3.0 | 2 | 3 | 0 |
| 3.25 | 7 | 8 | 3 |

*Note.* None of the fracture networks with $a = 2.25$ or $a = 3$ feature any backbone.

**Table 2**
*Rock and Fluid Properties*

| Property | Symbol | Unit | Background | Fracture |
|---|---|---|---|---|
| Shear modulus of dry frame | $\mu$ | GPa | 32 | 0.02 |
| Drained first Lamé parameter | $\lambda$ | GPa | 12.6 | 0.0116 |
| Permeability | $k$ | $m^2$ | $10^{-18}$ | $10^{-11}$ |
| Dynamic shear viscosity of the fluid | $\eta$ | Pa s | $10^{-3}$ | $10^{-3}$ |
| Porosity | $\phi$ | - | 0.06 | 0.5 |
| Bulk modulus of fluid | $K_f$ | GPa | 2.4 | 2.4 |
| Bulk modulus of solid grains | $K_s$ | GPa | 40 | 40 |
| Bulk modulus of dry frame | $K_b$ | GPa | 34 | 0.025 |

we solve the quasi-static poroelastic equations (Biot, 1941) formulated for solid displacement **u** and fluid pressure $p$ (Quintal et al., 2011) in the space-frequency domain

$$\nabla \cdot \boldsymbol{\sigma} = 0, \tag{2}$$

$$\nabla \cdot \left( -\frac{k}{\eta} \nabla p \right) + j\omega\alpha \nabla \cdot \mathbf{u} + j\omega \frac{p}{M} = 0, \tag{3}$$

with the components of the stress tensor $\boldsymbol{\sigma}$ being

$$\sigma_{mn} = 2\mu\varepsilon_{mn} + \lambda \left( \sum_{m=1}^{2} \varepsilon_{mm} \right) \delta_{mn} - \alpha p \delta_{mn}. \tag{4}$$

The imaginary unit $j$ is equal to $\sqrt{-1}$, and $\omega$ is the angular frequency. The Kronecker delta $\delta_{mn}$ is 1 for $m = n$ and 0 otherwise. The components of the strain tensor $\boldsymbol{\varepsilon}$ are related to the displacement **u** as follows:

$$\varepsilon_{mn} = \frac{1}{2} \left( \frac{\partial u_m}{\partial x_n} + \frac{\partial u_n}{\partial x_m} \right). \tag{5}$$

The parameters $M$ and $\alpha$ are defined as

$$\frac{1}{M} = \frac{\phi}{K_f} + \frac{\alpha - \phi}{K_s} \text{ and } \alpha = 1 - \frac{K_b}{K_s}. \tag{6}$$

The remaining parameters are given in Table 2.

We solve this set of equations using our own finite-element code for different boundary conditions depending on the type of the test. For the compressibility test, the rectangular sample is compressed by applying a harmonically oscillating vertical displacement of amplitude $\Delta u_y$ along its upper boundary. For the shear test, a horizontal oscillatory displacement of amplitude $\Delta u_x$ is applied in a similar way along the upper boundary of the sample. The amplitude of the applied displacement does not affect the resulting attenuation or modulus dispersion. We use a value of 1 μm, which is much smaller than the aperture of the fractures. The vertical as well as the horizontal displacement at the lower boundary is set to zero. For both tests, we apply periodic boundary conditions for the displacement and the fluid pressure and antiperiodic boundary conditions for the traction and the fluid flux (Jänicke et al., 2015), unless a specific boundary condition is defined for a given boundary. Note that the geometry of the fractures is also periodic with regard to the model boundaries.

The mesh used for the finite-element simulations is quadrilateral with small elements inside the fractures, while the elements outside the fractures are gradually increasing in size (Figure 2). The largest elements feature a side length of 4 mm, while the smallest elements, inside the fractures, have a side length of 0.0625 mm. Thus, a fracture aperture of 0.5 mm corresponds to the length of eight elements. The boundaries of the elements do not coincide with the boundaries of the fractures. In other words, an element can lie partially inside and partially outside a fracture. The material properties are specified on the quadrature points (Figure 2). This simplifies the meshing considerably, allowing for a reliable automated mesh generation. However, to

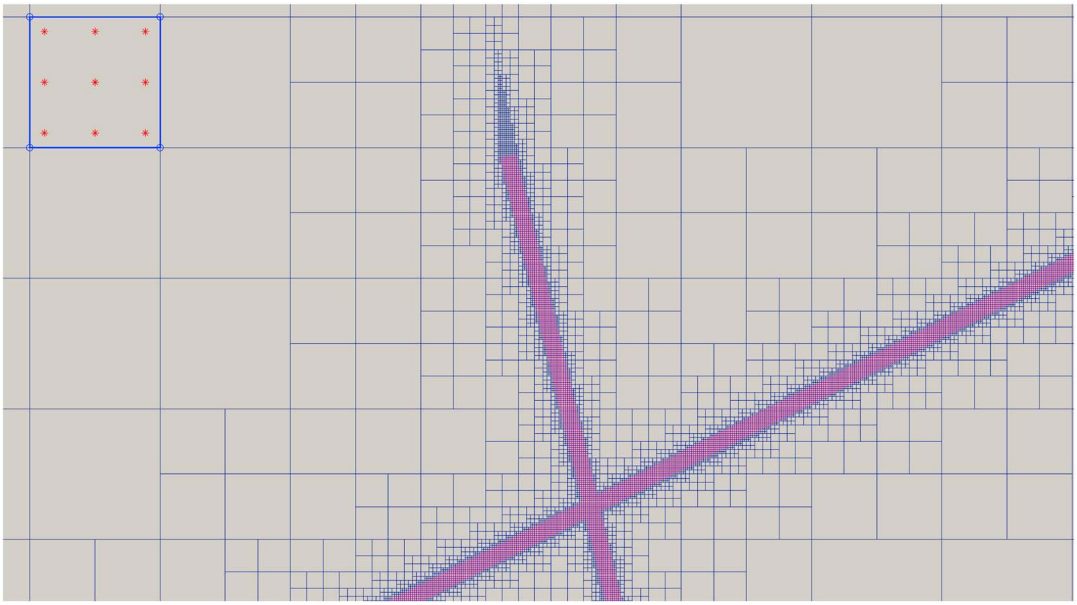

**Figure 2.** Detail of a mesh of two intersecting fractures. The red overlay identifies the position of the fractures. The highlighted element in the top left corner shows the locations of the quadrature points as red asterisks.

reduce stair-casing artifacts on tilted fractures resulting from this meshing strategy, the mesh needs to be fine enough inside the fractures, which is achieved with our choice of element size.

After completion of the finite-element simulations, we obtain the *P* and the *S* wave attenuation and the modulus dispersion by computing the complex *P* and *S* wave moduli $H(\omega)$ and $\mu(\omega)$, respectively. Thereby, we assume the samples to be isotropic, as the orientation of the fractures was drawn from an isotropic distribution. However, as creating the fracture networks is a stochastic process, it is possible that some individual fracture networks are slightly anisotropic. Nevertheless, we use the expression for isotropic samples to compute the complex moduli and attenuations. In the presence of weak anisotropy, this remains valid for a vertically incident seismic wave. Additional stress and strain components, which are negligible for a vertically incident seismic wave, are ignored. For the case of *P* waves we have

$$H(\omega) = \frac{\bar{\sigma}_{22}(\omega)}{\bar{\varepsilon}_{22}(\omega)}, \tag{7}$$

where $\bar{\sigma}_{22}(\omega)$ and $\bar{\varepsilon}_{22}(\omega)$ are the vertical components of the spatially averaged stress and strain tensor, respectively. Note that $\bar{\varepsilon}_{22}(\omega)$ is equal to $-\Delta u_y/L = -0.4$ for all the compressional tests. The *P* wave attenuation $1/Q_p$ is then given by (O'Connell & Budiansky, 1978)

$$\frac{1}{Q_p(\omega)} = \frac{\Im\{H(\omega)\}}{\Re\{H(\omega)\}}, \tag{8}$$

with $\Re$ and $\Im$ denoting the real and imaginary parts, respectively. For the dispersion analysis, we simply consider the real part of the complex *P* wave modulus $H(\omega)$.

Similarly, we obtain the complex *S* wave modulus $\mu(\omega)$ from the shear tests using the off-diagonal components of the average stress tensor $\bar{\sigma}_{12}$ and the average strain tensor $\bar{\varepsilon}_{12}$

$$\mu(\omega) = \frac{\bar{\sigma}_{12}(\omega)}{2\bar{\varepsilon}_{12}(\omega)}. \tag{9}$$

The factor of 0.5 stems from the Voigt notation (Mavko et al., 2009). Also here, $\bar{\varepsilon}_{12}(\omega)$ is known in advance and its value is $\Delta u_x/(2L) = 0.2$ for the shear tests. The attenuation of the *S* wave $1/Q_s$ is then given by

$$\frac{1}{Q_s(\omega)} = \frac{\Im\{\mu(\omega)\}}{\Re\{\mu(\omega)\}}. \tag{10}$$

The real part of the complex shear modulus $\mu(\omega)$ is used for the dispersion analysis.

In this approach, dynamic effects are neglected and all attenuation and modulus dispersion is attributed to pressure diffusion processes. Thus, the flow of the fluid at the pore-scale is laminar. We assume that fractures can be approximated by a poroelastic medium and their size is of the mesoscopic scale range. Furthermore, we assume that the sample corresponds to a representative elementary volume (REV) of the heterogeneous geological formation. As we consider stochastically generated fracture networks with periodic boundary conditions, the assumption that the sample is an REV tends to be satisfied if the tests are executed on a sufficiently large number of stochastic samples (Caspari et al., 2016). A detailed discussion regarding these assumptions and limitations is given by Rubino et al. (2014). Another limitation of our approach is that we can only consider 2-D samples at the moment. Appendix B provides a short discussion regarding the expected 3-D effects.

## 4. Results

### 4.1. Attenuation as a Function of Characteristic Exponent *a* of the Fracture Length Distribution and Fracture Density $d_a$

We consider three different values of the exponent $a$ and five different values of the fracture density $d_a$, which results in 15 different parameter combinations, of which three are presented in Figure 1. For each combination, we draw 20 fracture networks and compute the attenuation for each network at 41 different frequencies, which are logarithmically distributed between $10^{-4}$ and $10^6$ Hz. As each fracture network was subjected to a compressibility and a shear test, this results in 24, 600 separate computations. The material properties are given in Table 2 (e.g., Mavko et al., 2009; Quintal et al., 2014).

As we focus on the two FPD processes, (1) between the fractures and the background and (2) within connected fractures, we have chosen the physical rock properties such that these two processes are separated in terms of their dominant frequencies. However, this requires to simulate frequencies as high as $10^6$ Hz, where the quasi-static assumption is becoming invalid. In addition to the two FPD processes, also other attenuation mechanisms take place at these high frequencies. Inertia-related effects, such as the development of viscous boundary layers and classical Biot global flow, as well as scattering are neglected in this study.

Figures 3 and 4 show the frequency-dependent attenuation obtained from compression and shear tests, respectively, for the 15 parameter combinations. The bold black line represents the corresponding median. All attenuation curves feature two peaks. The first peak is associated with FPD from the fracture into the surrounding rock (e.g., Brajanovski et al., 2005), while the second one is caused by FPD between connected fractures (e.g., Quintal et al., 2014; Rubino et al., 2013). For some networks, the second peak is only discernible as a plateau. This is either caused by its proximity to the first peak and its comparatively low magnitude or by its broadness stemming from the contribution of multiple dominant length scales present in the fracture networks.

From the different realizations of the same length distribution (gray lines) it is evident that the variability of the magnitude of the second attenuation peak is increasing with decreasing fracture density $d_a$. This is the case for the *P* wave attenuation but even more so for the *S* wave attenuation. This is particularly extreme for a few fracture networks shown in Figures 4n and 4o, which feature very high attenuation associated with the second peak. An inspection of the corresponding fracture networks revealed that these seemingly erratic characteristics are caused by the presence of a few long fractures. At lower fracture densities, the presence of a few long fractures affects the fracture distribution (i.e., a lower number of short fractures will be present), and thus the attenuation, considerably.

To minimize the effect of these outliers for further interpretation, the median *P* wave attenuation and modulus dispersion for each length distribution are plotted in Figures 5a and 5b, respectively. The corresponding plots for the *S* wave attenuation and modulus dispersion are shown in Figures 5c and 5d, respectively. The low-frequency peak is located between $10^{-3}$ and 1 Hz, while the high-frequency peak is found between $10^2$ and $10^5$ Hz. For the *P* wave attenuation, and to a lesser degree for the *S* wave attenuation, the frequency of the first attenuation peak (FPD into the background) remains roughly at the same frequency for a constant fracture density $d_a$ and a changing characteristic exponent $a$. The characteristic timescale for FPD from the fractures into the background depends on the fracture length for noninteracting fractures (Galvin & Gurevich, 2006), which implies that the peak frequency would change as a function of the characteristic exponent $a$. This is not the case here, because, for the fracture densities considered, single fractures can no longer be

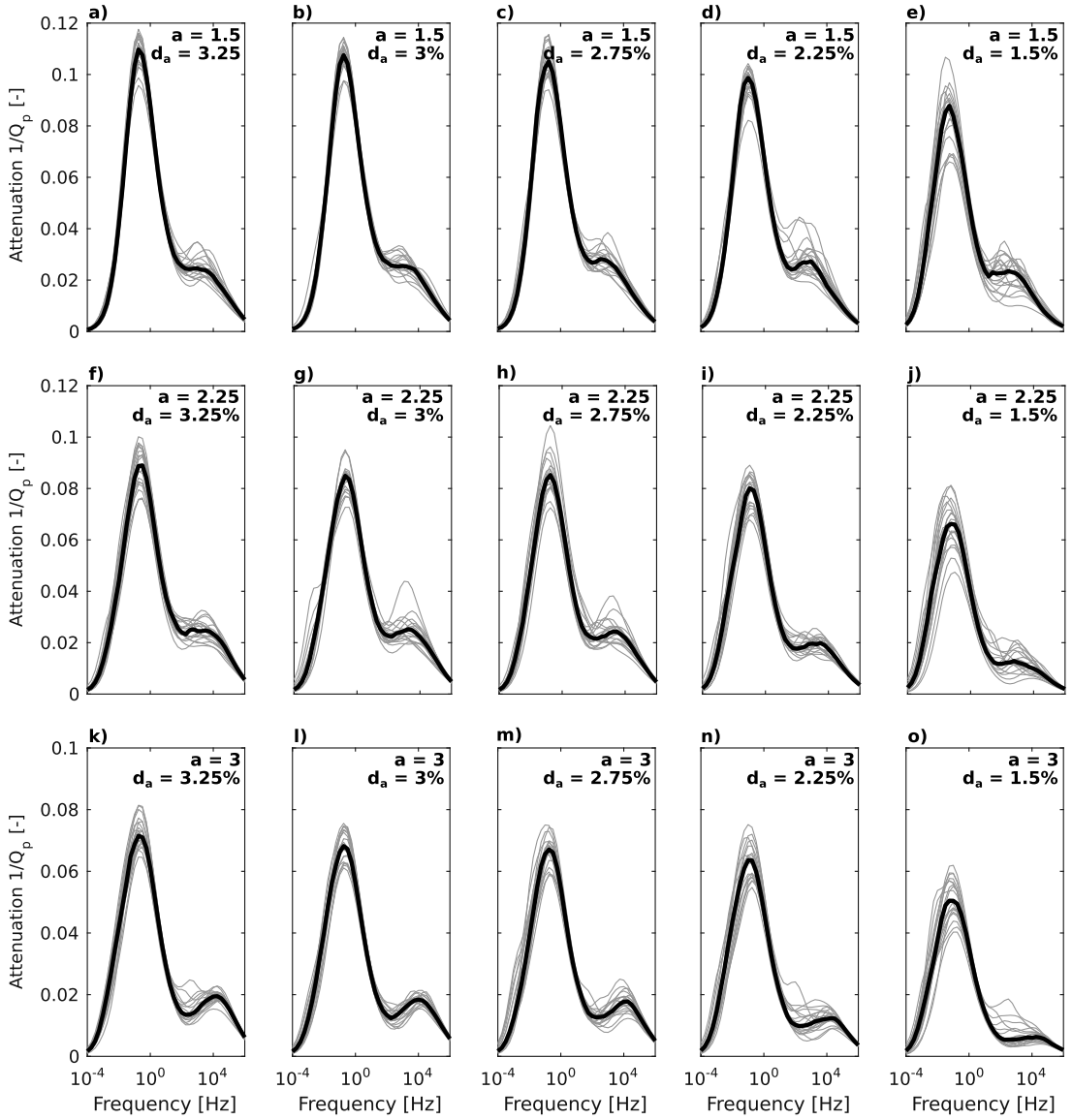


**Figure 3.** Attenuation curves obtained from compression tests for 15 different combinations of $a$ and $d_a$ (fine gray lines). The bold black line corresponds to the median.

considered as noninteracting and the characteristic timescale becomes dependent on the distance between the fractures, as has been shown for 1-D media (Brajanovski et al., 2005; White et al., 1975). Thus, the location of the low-frequency peak becomes dependent on the fracture density $d_a$ instead of the characteristic exponent $a$. For an increasing fracture density $d_a$, the average distance between the fractures decreases. Therefore, the characteristic timescale for this process decreases resulting in an increase in peak frequency (Figure 5a). Another effect which is associated with increasing fracture density is that fractures are more segmented and, thus, the scale of fracture-to-background FPD decreases, which again results in an increase of the peak frequency.

For *P* and *S* waves, the high-frequency peak shifts to lower frequencies when the exponent $a$ is decreased (Figures 5a and 5c). The characteristic length for FPD within connected fractures is the distance between the tip of a fracture and its connection with another one (Rubino et al., 2014). A decreasing value of $a$ results in a lower number of shorter fractures and thus in an increase of the characteristic timescale of this process, which in turn leads to a decrease of the peak frequency.

Both, the *P* and *S* wave moduli (Figures 5b and 5d) exhibit an overall decrease with an increase in fracture density $d_a$. The presence of more fractures weakens the medium and, therefore, lowers the modulus and

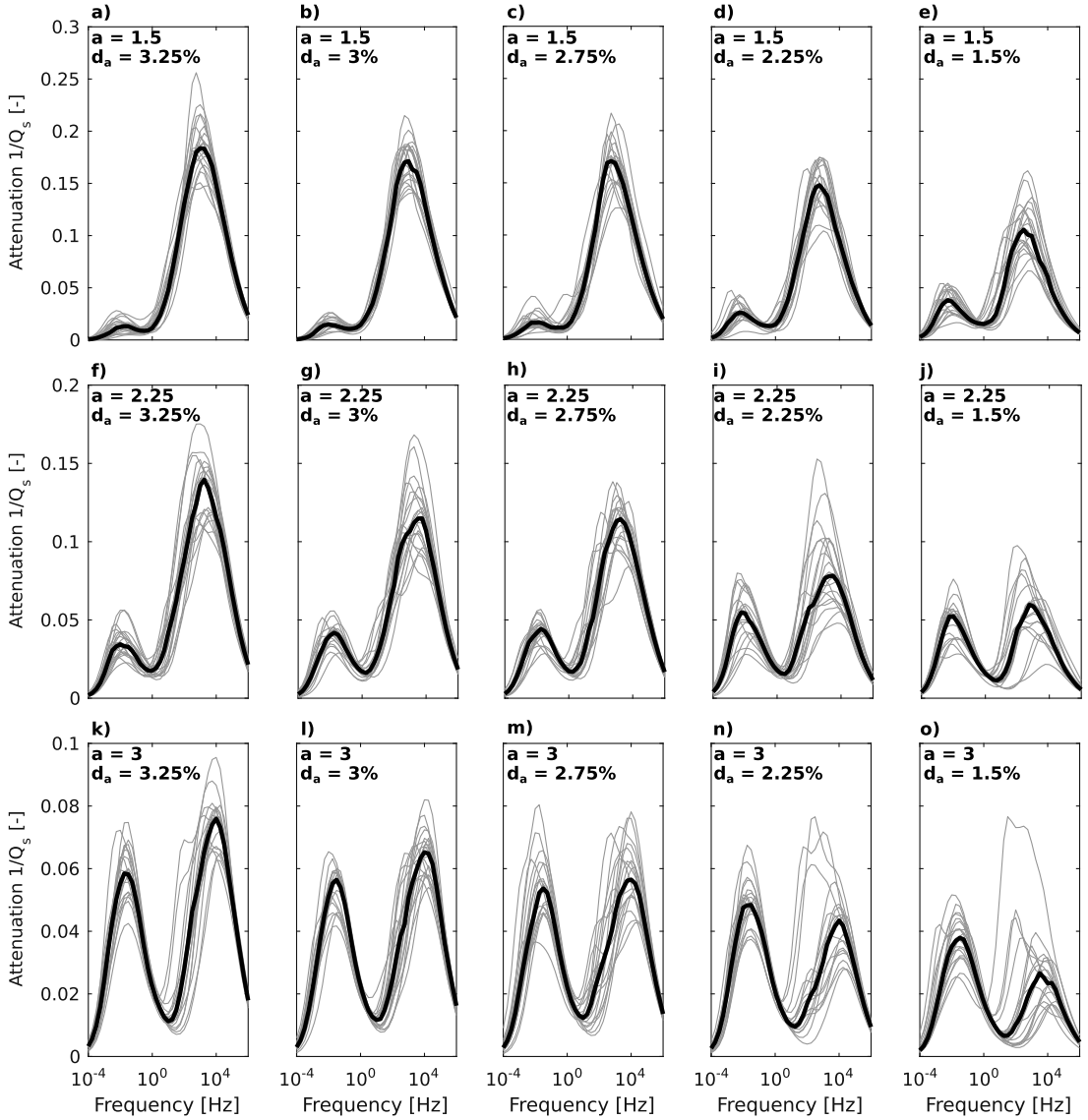


**Figure 4.** Attenuation curves obtained from shear tests for 15 different combinations of $a$ and $d_a$ (fine gray lines). The bold black line corresponds to the median.

the velocity. The degree of weakening of the effective elastic moduli differs considerably between the length distributions. At the same fracture density, the moduli are consistently lower for a decreasing exponent $a$. Thus, the effective moduli are not only sensitive to the fracture density but also to the fracture length. Longer fractures seem to weaken the medium more than the same volume fraction of shorter fractures. This difference between the length distributions is also reflected in the overall amount of attenuation, which is largest for scenarios with $a = 1.5$. For $P$ waves, the first peak exhibits the highest attenuation, whereas for $S$ waves, the second peak exhibits the highest attenuation, although, in this case, the relative importance of the two attenuation peaks depends more strongly on the fracture length distribution.

### 4.2. Attenuation as a Function of the Number of Fracture Connections

To facilitate the interpretation of attenuation in terms of fracture connectivity for the considered three length distributions, we picked the two peaks of the attenuation curves for each individual fracture network. The median and the range of the frequency of each peak as well as the median and the range of the magnitude of each peak are plotted in Figures 6a–6d for $P$ waves and in Figures 7a–7d for $S$ waves as a function of the number of fracture connections. Fracture networks with an exponent of $a = 1.5$ contain at the two lowest fracture densities on average a slightly larger number of connections, whereas at the two highest fracture densities the number of connections is larger for networks with an exponent $a = 3$.

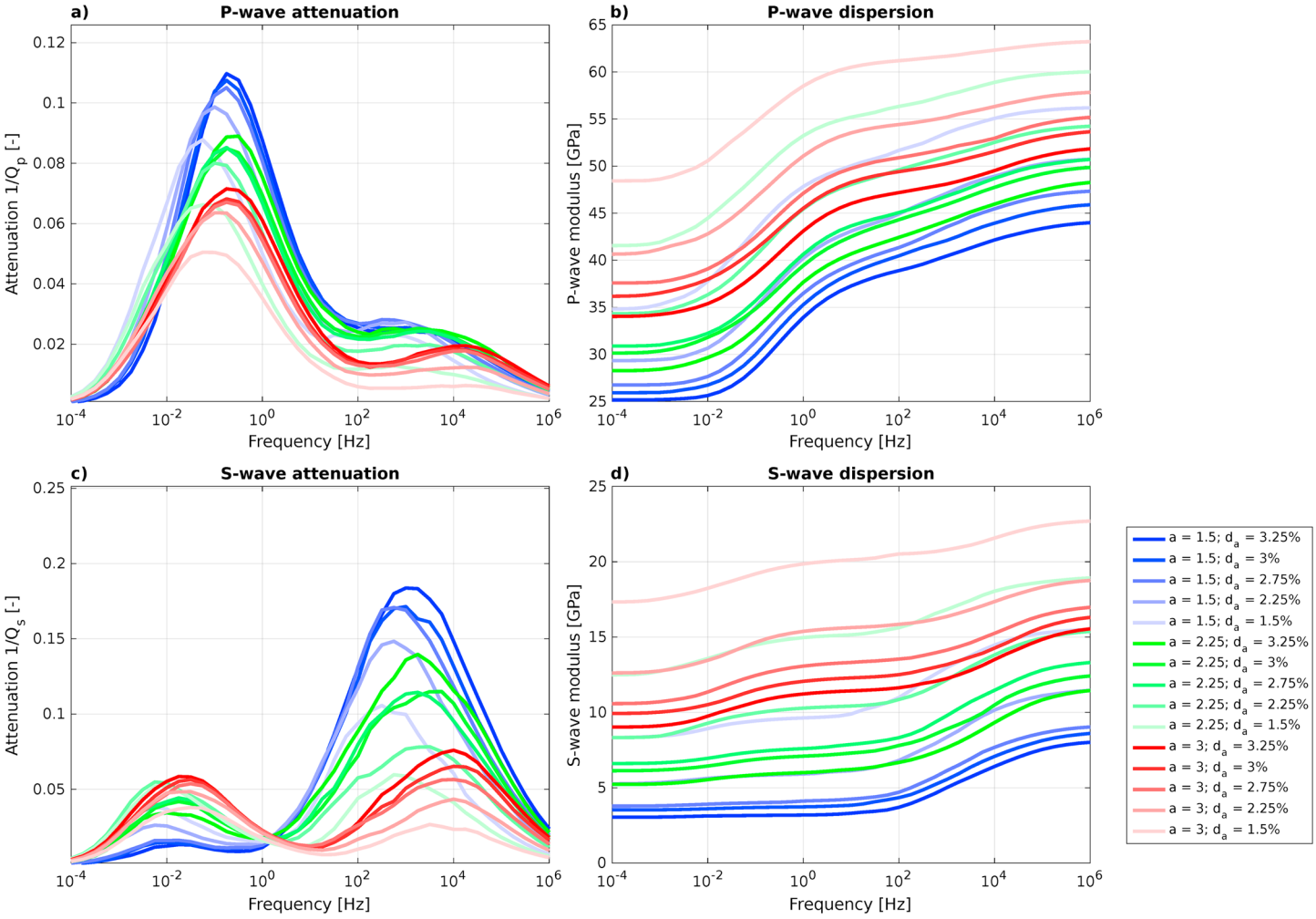


**Figure 5.** (a) Median *P* wave attenuation $1/Q_p$, (b) median *P* wave modulus dispersion, (c) median *S* wave attenuation $1/Q_s$, and (d) median *S* wave modulus dispersion for the 15 parameter combinations considered.

However, only the magnitude and frequency of the attenuation peaks may not characterize the two manifestations of FPD comprehensively as information about the shape of the peaks is not considered. For example, a narrow peak might have the same peak attenuation as a broad peak, but the frequency range, over which the process prevails, could be quite different. Therefore, we decompose the attenuation curves into two independent components associated with the corresponding attenuation peaks and compute the area below the separated curves (Appendix A). The mean and the range of this quantity is plotted as a function of the number of fracture connections in Figures 6e and 6f and Figures 7e and 7f for *P* and *S* waves, respectively. The area under the attenuation curves and the magnitude at the peak frequencies exhibit the same pattern. This consistency between the two quantities indicates that they describe the prevailing physical processes adequately.

For most of the scenarios considered, the magnitude of the first attenuation peak and the area under the attenuation curve increase with the fracture density and the number of fracture connections. An exception is the *S* wave attenuation associated with exponents $a = 1.5$ and, in part, $a = 2.25$ (Figures 7c and 7e), where the magnitude of the first peak decreases with an increase of fracture connections. For these length distributions, longer fractures are more numerous and the networks contain larger connected clusters, which in the case of $a = 1.5$ leads to the formation of backbones (Table 1). It seems that for this *S* wave scenario, the FPD process occurs mainly within these internally connected clusters for a sufficiently large number of connections, and thus, it mainly contributes to the second attenuation peak.

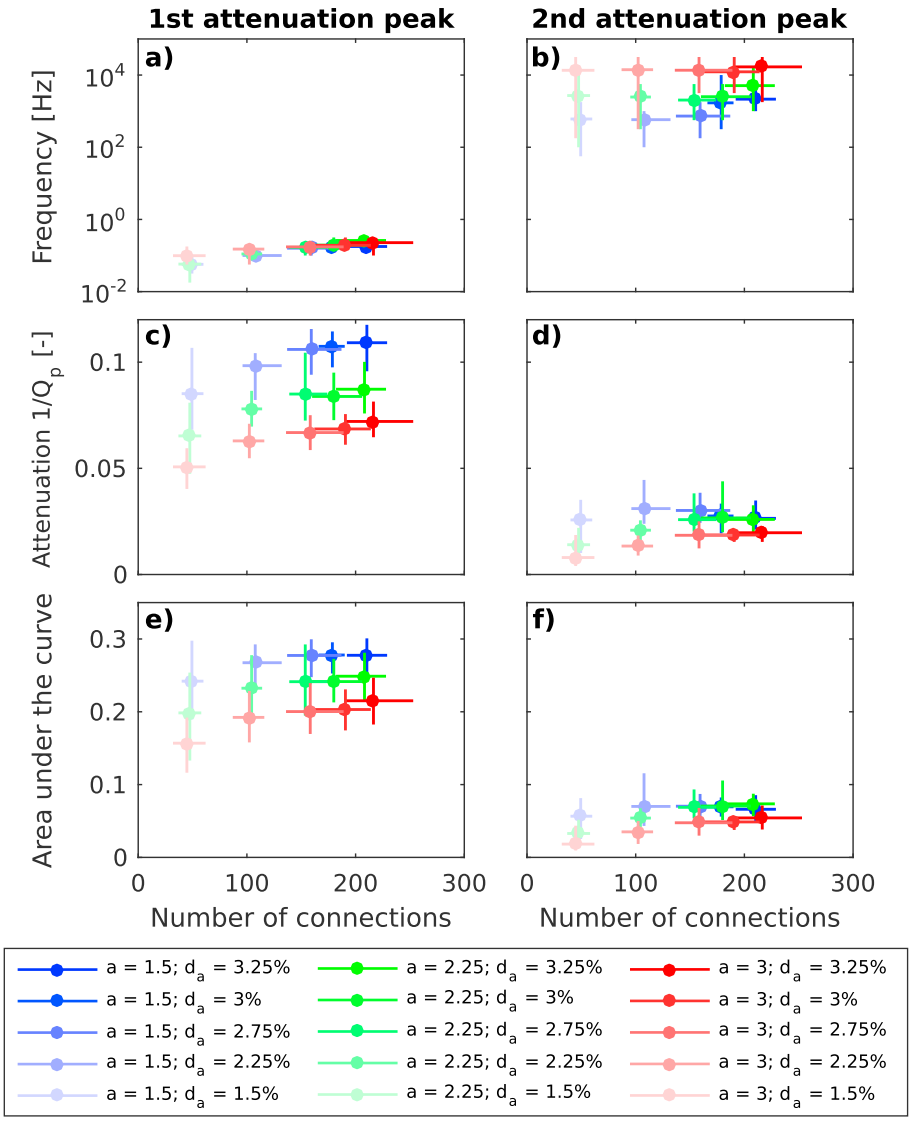


**Figure 6.** Key results of the compression tests showing the attenuation trends with number of fracture connections: Average frequencies associated with (a) the first and (b) the second attenuation peak; average maximum attenuation associated with (c) the first and (d) the second attenuation peak; area under the attenuation curve for a logarithmic frequency axis for (e) the first and (f) the second attenuation peak. The range of observed values is denoted by orthogonal lines. The strength of the color is proportional to the corresponding fracture density.

Another interesting feature is that for the lowest fracture density the first *S* wave attenuation peak is quite similar in magnitude for the three considered length distributions. For the other cases, the difference between the magnitudes of attenuation at the same fracture density becomes larger. For *P* waves this difference is roughly constant at all densities (Figures 6c and 6e) and cannot be explained by the slight differences in the number of fracture connections between the distributions. Hence, the larger connected clusters for $a = 1.5$ and $a = 2.25$ and the backbones for $a = 1.5$ may be responsible for this observed difference as well. Overall, we can summarize that the magnitude of the first attenuation peak for both *P* and *S* waves is sensitive not only to the fracture density but also to the length distribution and, possibly, to internally connected clusters.

As it is mostly the case for the lower-frequency peak, an increase in the number of fracture connections is associated with an increase of the magnitude of the second peak as well as an increase of the area under the attenuation curve. However, the behavior of the attenuation trends for the second peak is quite different for *P* and *S* waves. While for all length distributions the *S* wave attenuation increases linearly and strongly with the number of fracture connections, the *P* wave attenuation first rises and then levels out. For $a = 1.5$, the *P*

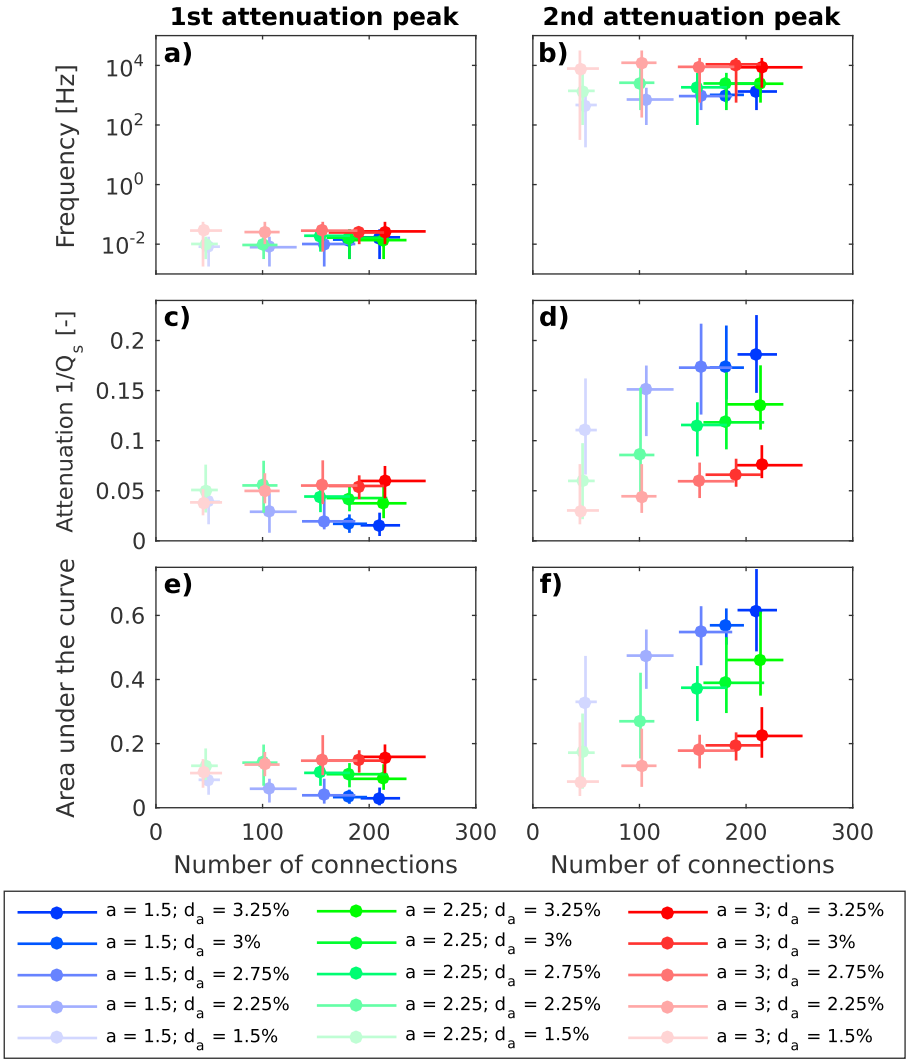


**Figure 7.** Key results of the shear tests showing the attenuation trends with number of fracture connections: Average frequencies associated with (a) the first and (b) the second attenuation peak; average maximum attenuation associated with (c) the first and (d) the second attenuation peak; area under the attenuation curve for a logarithmic frequency axis for (e) the first and (f) the second attenuation peak. The range of observed values is denoted by orthogonal lines. The strength of the color is proportional to the corresponding fracture density.

wave attenuation even slightly decreases at fracture densities above $d_a = 2.75\%$. For these cases, a significant amount of the considered fracture networks have a connected backbone (Table 1), which means that they are close to the percolation threshold. This in turn suggests that the *P* wave attenuation may be sensitive to the percolation characteristics of a fracture network. For *S* waves, the attenuation magnitude consistently increases with decreasing *a* and the difference in magnitude between different values of *a* slightly increases with fracture density.

### 4.3. Physical Explanation of the Attenuation Behavior

To gain a better understanding of the physical processes causing the observed attenuation trends as function of the number of fracture connections, we inspect fluid pressure fields in response to the applied numerical tests for selected networks in Figures 8 and 9 at frequencies associated with the lower-frequency peak, the minimum between the two attenuation peaks, and the highest frequency considered in our simulations ($10^6$ Hz).

In the high-frequency limit of the FPD process, the maximum fluid pressure gradients are induced in the medium as an instantaneous response to the applied displacements. The highest frequency in our simulations

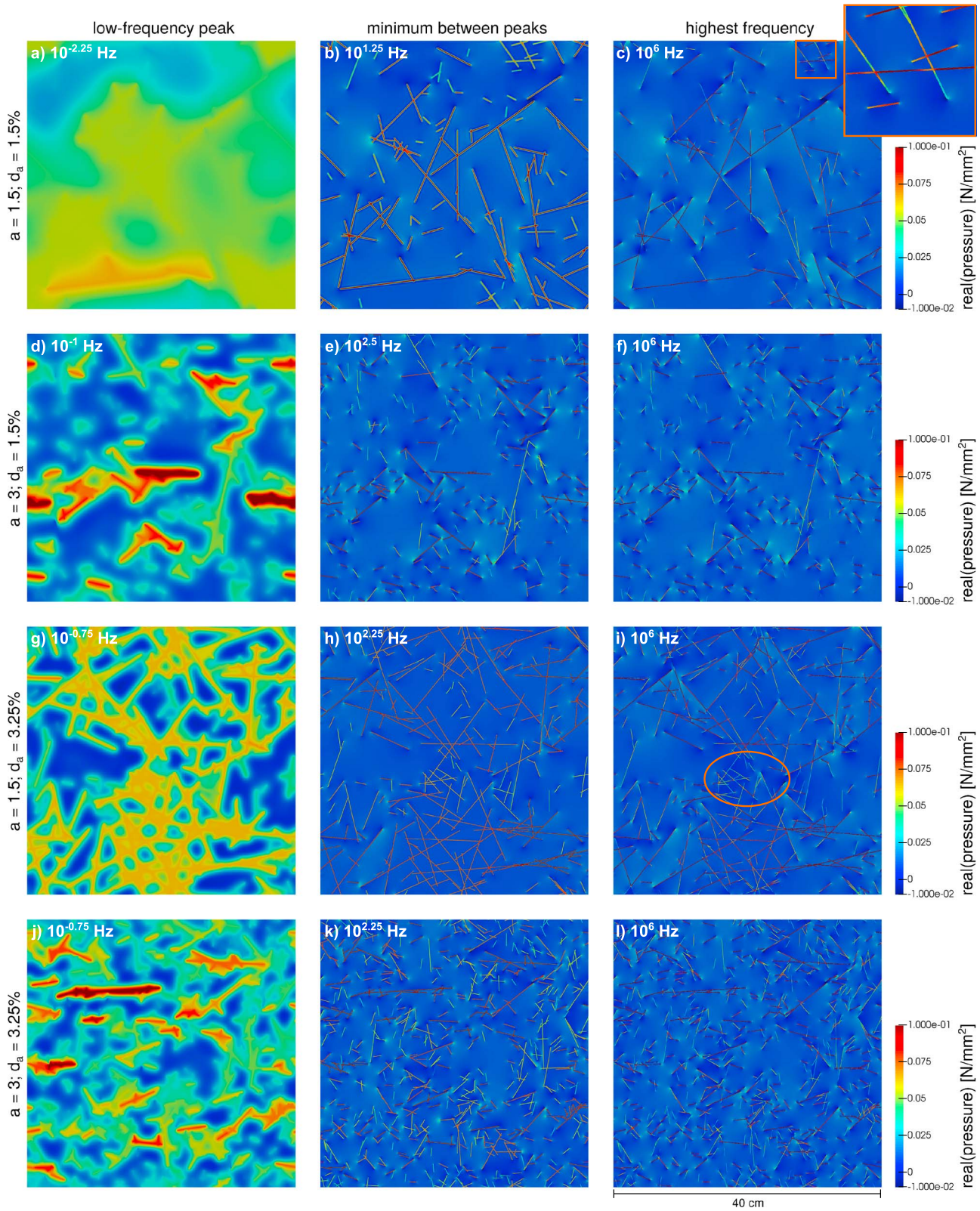


**Figure 8.** Fluid pressure distribution of compression tests for four fracture networks with different length distributions. The fluid pressure is shown (a, d, g, and j) at the frequency of the low-frequency peak, (b, e, h, and k) the frequency of the trough between the two peaks, and (c, f, i, and l) the highest considered frequency. The inset in Figure 8c illustrates the detailed pressure distribution in the fractures within the orange square. The orange ellipse in Figure 8i highlights a shielding zone.

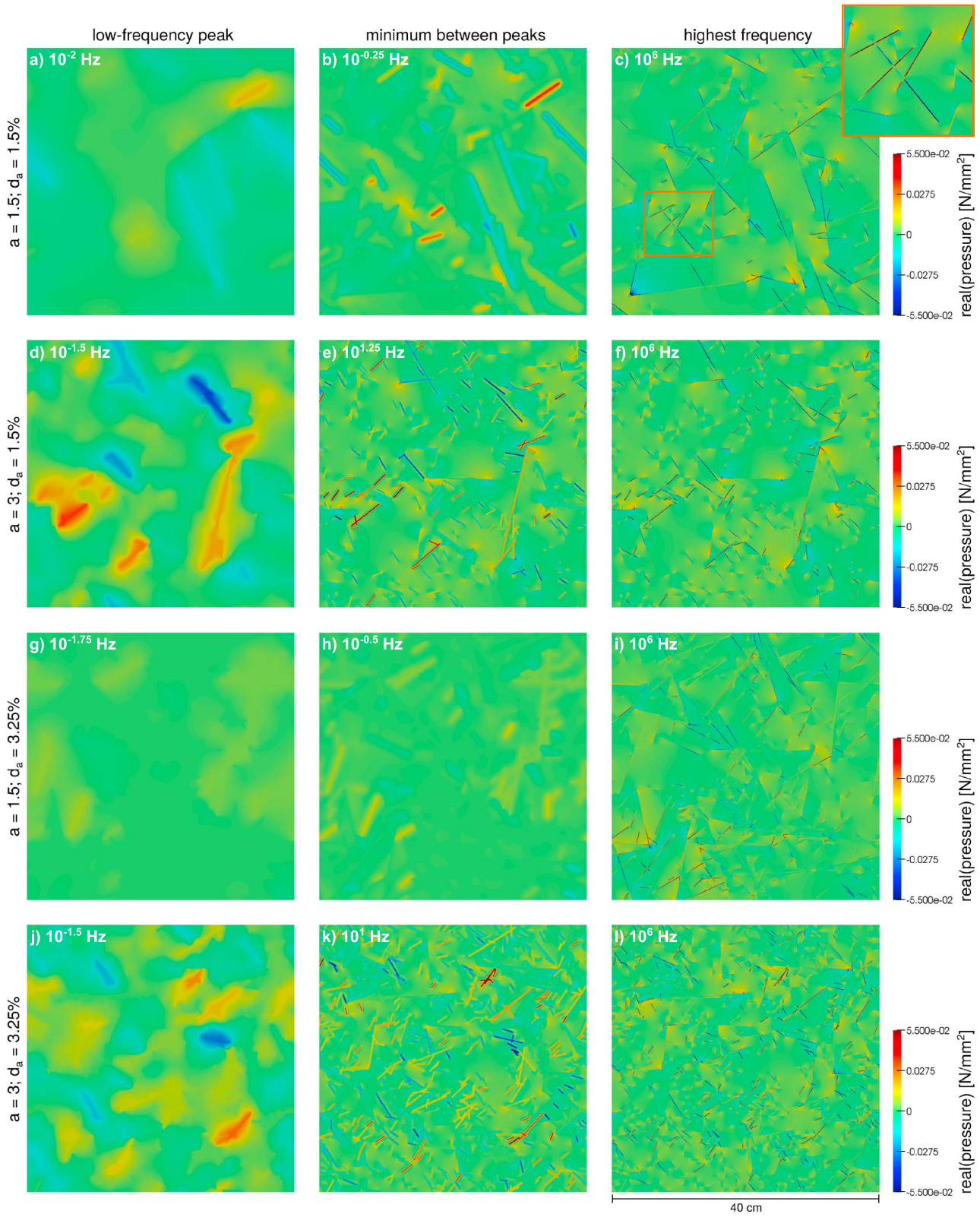


**Figure 9.** Fluid pressure distribution of shear tests for four fracture networks with different length distributions. The fluid pressure is shown (a, d, g, and j) at the frequency of the low-frequency peak, (b, e, h, and k) the frequency of the trough between the two peaks, and (c, f, i, and l) the highest considered frequency. The inset in Figure 9c illustrates the detailed pressure distribution in the fractures within the orange square.

does not quite reach this limit but provides a good indication of the magnitude of the fluid pressure gradients for the various scenarios (Figures 8c, 8f, 8i, and 8l and 9c, 9f, 9i, and 9l). The magnitude and spatial distribution of these gradients depend on the compliance contrast between fractures and background medium, the fracture orientation with respect to the applied displacement, and the elastic interaction of fractures with each other due to their geometrical arrangement. The attenuation magnitude resulting from FPD is directly proportional to the induced fluid pressure gradients as can be seen in the poroelasticity theory of Biot (1962). There, the dissipation function is written as a quadratic function of the fluid velocity, which, according to Darcy's law, is proportional to the pressure gradient. For the highly permeable fractures and low-permeability background considered here, the fracture-to-fracture FPD occurs on much shorter timescales, and thus at higher frequencies, than fracture-to-background FPD. Hence, the fluid pressure fields at the highest frequency govern the fracture-to-fracture FPD processes, while the fluid pressure fields at the other displayed frequencies predominantly govern fracture-to-background FPD (Figures 8 and 9). An additional controlling factor for fracture-to-background FPD is the fracture surface area over which the diffusion process takes place. For fracture-to-fracture FPD an additional factor is the available fluid storage volume of the connected fractures (Vinci et al., 2014).

#### 4.3.1. Fracture-to-Fracture FPD

For *P* waves, the induced fluid pressure inside the fractures is positive in a compression cycle and negative in a dilatation cycle. Here we look at the real part of the fluid pressure, which in time domain corresponds to the maximum of the applied compression. Therefore, we observe predominately positive fluid pressures (Figures 8c, 8f, 8i, and 8l), with the highest values in horizontal fractures and the lowest in vertical fractures. Thus, fracture-to-fracture FPD will cause the strongest attenuation due to intersecting fractures of these two predominant inclinations (Quintal et al., 2014). A corresponding example is shown in the inset of Figure 8c. However, the second attenuation peak corresponding to this manifestation of FPD is rather small in our simulations (Figure 5a). The reason is that due to the isotropic distribution of fracture orientations, it is rather unlikely to get a significant amount of quasi-orthogonally intersecting fractures with one fracture being parallel and the other one perpendicular to the applied displacement.

For *S* waves, the fluid pressure inside the fractures is either positive or negative depending on the orientation of the fracture with respect to the shear displacement (Rubino et al., 2017). These positive and negative fluid pressures occur in the positive as well as in the negative cycle of the shear perturbation due to a change of shape of the sample in a shear test. Therefore, the resulting fluid pressure gradients between neighboring and intersecting fractures (Figures 9c, 9f, 9i, 9l, and inset in Figure 9c) can get rather large. Thus, for the given networks with isotropic fracture orientations, fracture-to-fracture FPD and the resulting attenuation is more significant for *S* waves than for *P* waves (Figures 5a and 5c).

Another striking difference, described in the previous section, between the second attenuation peak of *P* and *S* waves is the attenuation trend as a function of fracture connections. At low fracture densities the attenuation increases for both wave types with an increase in fracture connections. Conversely, at high densities, the *P* wave attenuation reaches a plateau or even decreases slightly, while the *S* wave attenuation continues to linearly increase. The linear increase of attenuation for fracture-to-fracture FPD with the number of connections for *S* waves (Figure 7d) can be explained by an increase of the fluid storage volume since more and more connected fractures contribute to the FPD process. The same reasoning can be applied to the *P* wave attenuation at low fracture densities, although it does not explain the behavior at high fracture densities. There are two possible mechanisms which may counteract the attenuation increase due to a larger fluid storage volume. A close inspection of the fluid pressure fields reveals certain areas with lower induced fluid pressures within the fractures than on average (orange ellipse in Figure 8i). As known from elastic studies at high fracture densities, we have strong interactions between fractures resulting in so-called shielding and amplification zones (e.g., Kachanov, 1992). The former lead locally to zones with reduced deformation and thus lower fluid pressure gradients and smaller contributions to the overall attenuation. Such a shielding zone is observed inside the orange ellipse in Figure 8i. A different process at play is the following: The growing number of small and isolated fractures associated with large fracture densities absorb more and more of the deformation energy without significantly contributing to fracture-to-fracture FPD. In this way, these small fractures diminish the compressibility contrast between the background and the connected fractures. Correspondingly, the latter are compressed less and the fluid pressure gradients between intersected fractures are reduced, which in turn decreases fracture-to-fracture FPD. The first mechanism (shielding zones) might be more pertinent for networks characterized by a smaller exponent *a* and the second process (small and isolated fractures) for networks with a larger exponent *a*, where more small fractures are present.

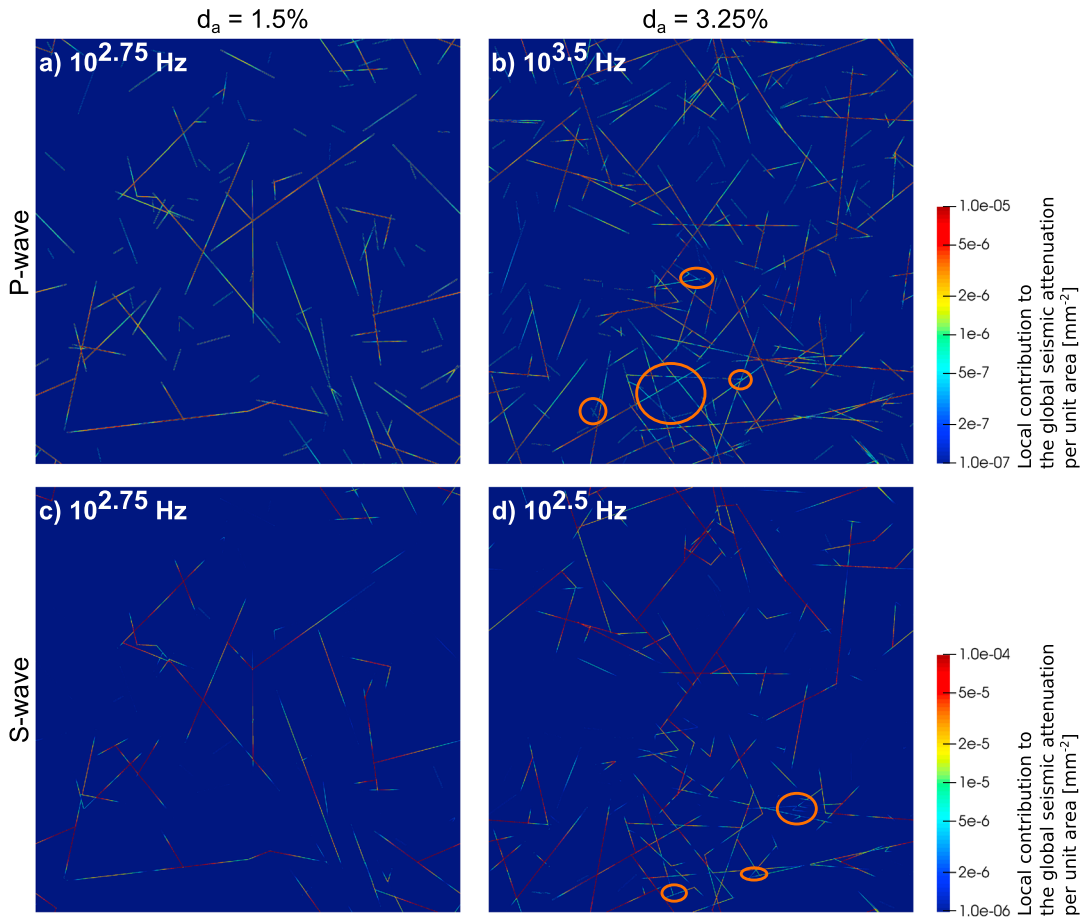


**Figure 10.** Local contribution to the overall seismic attenuation per unit area (Solazzi et al., 2016) at the frequency of the second attenuation peak for (a, b) *P* waves and (c, d) *S* waves for a fracture network with a fracture density of 1.5% (Figures 10a and 10c) and a fracture density of 3.25% (Figures10b and 10d). The characteristic exponent *a* is 1.5. The orange ellipses identify areas of connected fractures featuring a low local contribution to the overall seismic attenuation.

To further investigate the different *P* and *S* wave trends of the second attenuation peak and the corresponding role of the competing effects associated with the gain in fluid storage volume on one side and shielding zones or isolated fractures on the other hand, we show in Figure 10 the local contribution to the overall seismic attenuation per unit area (Solazzi et al., 2016) for specific fracture networks with $a = 1.5$. The frequency corresponds to that of the second attenuation peak and fracture densities of 1.5% and 3.25 %. For both fracture densities, the local contribution to the overall seismic attenuation is up to one order-of-magnitude higher for *S* waves than for *P* waves as a result of the larger fluid pressure gradients associated with the former. We have seen that for *P* waves the attenuation is approximately the same for fracture densities of 1.5% and 3.25% (Figure 6d), which in turn implies that the average attenuation per fracture must have decreased with increasing fracture density. At a fracture density of 3.25%, we observe for both wave types more areas of intersecting fractures with lower magnitudes of the local contribution to the overall attenuation than at a fracture density of 1.5%, and this effect seems to be more pronounced for *P* waves than *S* waves (orange ellipses in Figure 10). This confirms that the S-wave attenuation increases with increasing fracture density because it is controlled by the increased fluid storage volume, whereas the *P* wave attenuation reaches a plateau with increasing fracture density because it is more strongly affected by fracture interactions. However, Figure 10 does not allow to draw conclusions about single isolated fractures diminishing the compressibility contrast.

#### 4.3.2. Fracture-to-Background FPD

To understand the attenuation trends associated with the fracture-to-background FPD, we first need to reexamine the fracture-to-fracture FPD expressed in the second attenuation peak. For *P* and *S* waves, the second attenuation peak is larger for networks with a length distribution exponent of $a = 1.5$ as compared to networks

characterized by $a = 3$. The reason is that the former networks contain larger connected clusters at all fracture densities and less isolated small fractures, which results in a larger connected fluid storage volume. As a consequence, for networks characterized by $a = 1.5$ at the frequency corresponding to the minimum between the two attenuation peaks, the fluid pressure within the fractures is on average more equilibrated and similar in magnitude (Figures 8b, 8h, 9b and 9h) than for networks characterized by $a = 3$ (Figures 8e, 8k, 9e and 9k). These connected clusters play a role for fracture-to-background FPD.

For *P* waves, all three network types ($a = 1.5\%$, $a = 2.25\%$, and $a = 3.25\%$) feature relatively large remaining fluid pressure gradients between fractures and background, which in turn determine the magnitude of the first attenuation peak. Although we observe very high local gradients for small quasi-horizontal isolated clusters or fractures for $a = 3$ (Figures 8d and 8e, and 8j and 8k), the first attenuation peak is much larger for networks with $a = 1.5$. This is due to the larger sample-spanning clusters or backbones for $a = 1.5$ (Figures 8a and 8b, and 8g and 8h), which increase the contributing surface area over which fracture-to-background FPD takes place, due to the inclusion of quasi-vertical connected fractures. In other words, if the quasi-vertical fractures were not connected to other fractures, the fluid pressure gradient between the quasi-vertical fractures and the background would be much lower.

Conversely, for *S* waves, the induced positive and negative fluid pressures between fractures of different orientations cancel each other out more and more through fracture-to-fracture FPD with an increase of the number of fracture connections and the cluster size. Especially for networks characterized by $a = 1.5$, the remaining fluid pressure gradients between background and fractures become negligible (Figures 9g and 9h). This explains the trend of decreasing attenuation with the increasing number of connections for fracture-to-background FPD observed in Figures 7c and 7e.

## 5. Discussion

For simplicity, we considered isotropic networks and the fracture aperture as well as the material parameters were kept constant, which is most likely having an impact on the magnitudes and trends of the FPD mechanisms. Furthermore, although the chosen aspect ratios are realistic for fractured rocks, the maximum and minimum fracture length as well as the size of the fractured domain had to be chosen based on computational constraints, which in turn raises some questions with regard to their realism. The timescales (frequency range), at which FPD mechanisms prevail, directly scale with the characteristic length scales of the medium (e.g., Brajanovski et al., 2005; Quintal et al., 2014; Rubino et al., 2013), that is, fracture length and spatial correlation of the fracture networks as well as the hydraulic diffusivity, which in turn is determined by the permeability of the background and fractures. Thus considering longer fractures will shift both mechanisms toward lower frequencies, whereas considering a larger hydraulic diffusivity will shift the mechanisms to higher frequencies. This direct relation between fracture size, hydraulic diffusivity and the characteristic timescale (frequency) hence offsets the potential limitations imposed by choosing the size based on computational constraints.

Another limitation is that the numerical upscaling method applied to obtain attenuation is based on quasi-static poroelasticity and hence does not account for inertia-related effects and their impact on attenuation. The quasi-static assumption is violated for our specific scenarios at frequencies above 8 kHz with regard to the fracture material. This does not affect FPD processes in the background but may affect fracture-to-fracture flow at these frequencies. A detailed discussion of this subject is provided by Rubino et al. (2014).

Another attenuation mechanism, which is not considered in this study, is scattering, which, for the considered medium parameters, takes place at frequencies above $10^4$ Hz for *P* waves and above $10^3$ Hz for *S* waves. Although this mechanism will not directly interfere with the diffusion process (Gurevich et al., 1997; Novikov et al., 2017), it will make the observation of pressure diffusion processes from seismic measurements more difficult. A solution would be to separate scattering from intrinsic attenuation (Pevzner et al., 2012; Wu, 1985).

## 6. Conclusions

In this study, we analyzed the sensitivity of *P* wave and *S* wave attenuation in porous fluid-saturated fractured media due to two manifestations of the FPD mechanism, (1) fracture-to-background FPD and (2) fracture-to-fracture FPD. The considered fracture networks are isotropic and drawn from power law length distributions for three different characteristic exponents covering a range of typical scenarios at five different

fracture densities. Our results show that the attenuation magnitudes and their relative importance for the two manifestations of FPD arising in fractured media depend on the wave mode, the fracture density, and the fracture length distribution.

For the considered isotropic distributions of fracture orientations, fracture-to-fracture FPD is more significant for *S* waves than for *P* waves, since for the former the induced pressure gradients between fractures are larger than for the latter. For both wave types the attenuation increases with fracture density and decreasing characteristic length exponent *a* until we approach the percolation threshold of the networks. At this threshold, the attenuation for *S* waves continues to increase for all characteristic length exponents and fracture densities. This is due to an increasing number of fracture connections and, thus, a larger fluid storage volume that takes part in the FPD process resulting in more attenuation. However, for *P* waves at small values of the exponent *a*, for which with increasing density more and more large fracture clusters occur, the increase in storage volume is counteracted by the competing effect of mechanical fracture interactions. This in turn results in smaller pressure gradients and thus less attenuation.

The large connected fracture clusters observed for low values of the characteristic length exponent *a* are also responsible for the differing attenuation trends in the presence of fracture-to-background FPD. On one hand, they explain the larger *P* wave attenuation for $a = 1.5$ (networks dominated by long fractures) compared to $a = 3$ (networks dominated by short fractures) due to the inclusion of more fractures into the process. On the other hand, the clusters are responsible for the decreasing *S* wave attenuation trend for this FPD process at a characteristic exponent *a* of 1.5, since, for more and more connected clusters, the remaining fluid pressure gradients between fractures and the embedding background become negligible.

We can conclude that for both wave modes attenuation is sensitive to the length distribution and the associated connectivity properties of the fracture network. For the considered networks, the high-frequency attenuation peak of *S* waves appears as the strongest and most consistent indicator of an increasing number of fracture connections. But also the opposing trends for *P* and *S* waves for fracture-to-fracture and fracture-to-background flow might be used as an indicator for changes of fracture connectivity. However, establishing a direct relation to the hydraulic conductivity of the probed fractured material remains difficult, since the attenuation depends on the number of local connections, the size of the clusters, and the degree of elastic interaction between fractures, and not necessarily on the existence of a backbone. Thus, attenuation due to FPD contains information with regard to the local connectivity of a fracture network, but not with regard to the global connectivity, which governs the hydraulic conductivity of fractured media. Nevertheless, local connectivity information is potentially useful for identifying regions of high fracture connectivity, often referred to as sweet spots in hydrocarbon or geothermal exploration. Systematic and reliable mapping of sweet spots would allow to steer the boreholes into the most productive regions, thus reducing the need for hydraulic fracturing or other forms of reservoir stimulation.

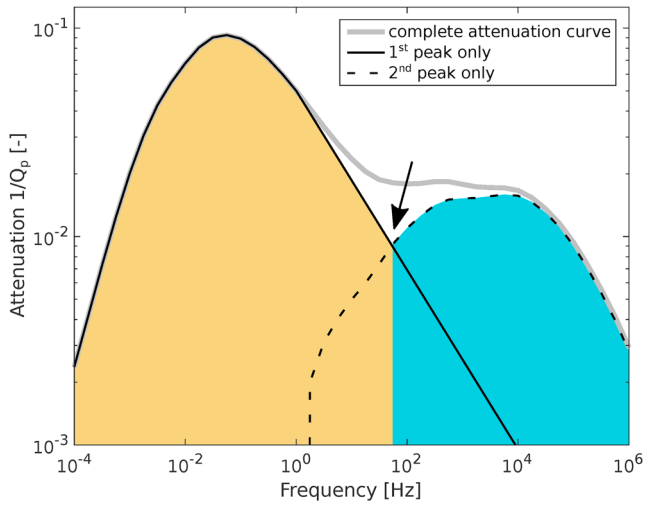


**Figure A1.** The complete attenuation curve (bold gray line) of a fracture network is split into a low-frequency peak (black solid line) and a high-frequency peak (black dashed line). The black arrow indicates the crossing of the two curves, which serves as bound for the integral. The areas under the curve associated with the low-frequency and the high-frequency peak are colored in yellow and blue, respectively.

## Appendix A: Isolation of the Two Attenuation Peaks

The decomposition of the attenuation curve into two independent components is illustrated in Figure A1. Starting from the complete attenuation curve in a double-logarithmic scale (bold gray line), we extrapolate the slope of the low-frequency peak toward higher frequencies. Replacing the part of the curve after the low-frequency peak with the extrapolated curve results in an approximation of the low-frequency peak (black solid line). The approximate attenuation curve associated with the high-frequency peak (black dashed line) is then obtained by subtracting the previously inferred curve for the low-frequency peak from the complete attenuation curve. Clearly, these approximations deviate considerably from the true attenuation outside regions associated with the respective peaks. When estimating the area under the curve of the low-frequency peak, we therefore consider only frequencies between the starting frequency and the frequency where the two curves cross (black arrow). In Figure A1, the area associated with the low-frequency peak is colored

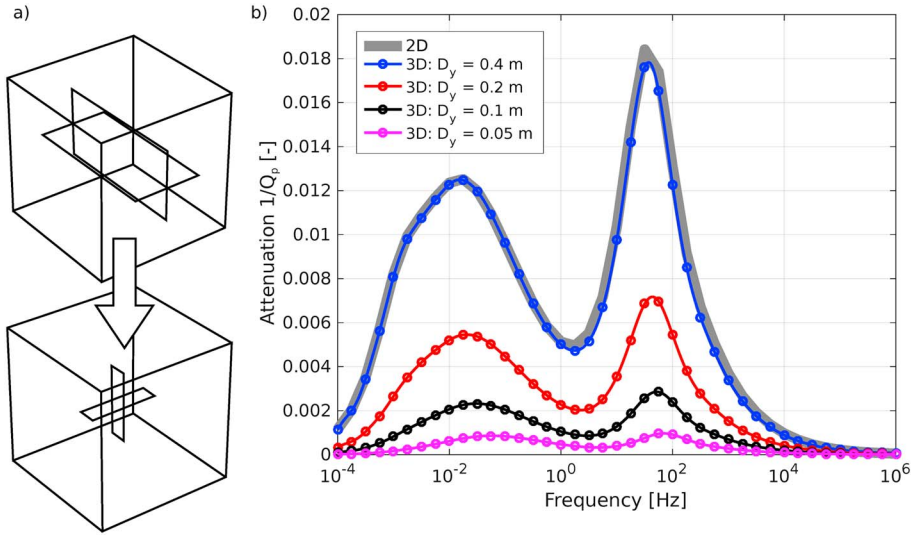


**Figure B1.** Comparing 2-D simulations of two crossing fractures with the corresponding 3-D simulations. The length of the 3-D sample is 0.4 m in each direction. The length of the fracture in the third dimension is given by $D_y$. (a) Geometry of the sample with the fractures. On the top plot, the fractures are as long in the third dimension as the length of one side of the sample. The bottom plot shows the same fractures with a limited extent in the third dimension. (b) Attenuation for the 2-D sample and the 3-D sample with different length scales of the fracture in the third dimension.

in yellow. For the high-frequency peak, we correspondingly integrate from the frequency where the two curves cross up to the largest frequency available (blue area).

## Appendix B: Considerations Regarding 3-D Effects

Our 2-D samples considered so far correspond in 3-D to samples whose geometry is infinite in the out-of-plane direction. In other words, the fractures would be infinitely long in the third dimension. In reality, however, fractures are finite in all directions. An analytical expression for simple geometries to correct 2-D numerical attenuation curves to the corresponding response of 3-D finite-sized fractures was recently derived by Barbosa et al. (2017). To explore how our results differ from those of a 3-D scenario, we perform a simple 3-D numerical simulation of two fractures intersecting each other orthogonally (Figure B1a). The aperture of the fractures is 0.1 mm and their length is 0.2 m. A side of the cube is, as for the 2-D samples, 0.4 m long. The physical rock properties are the same as for the 2-D simulations. A vertical compression test with the same boundary conditions as before is carried out on this 3-D sample and the results are compared to those of a 2-D sample consisting of the front face of the geometry depicted in the top plot of Figure B1a. For these simulations, we use a commercial software package and the mesh, which follows the fracture geometry, uses triangular elements for the 2-D simulation and tetrahedral elements for the 3-D simulations.

First, we compare the 2-D result for this geometry (gray curve in Figure B1b) with a 3-D simulation with the fractures being as long as the cube in the third dimension (blue curve in Figure B1b). The two curves agree well, thus, illustrating that our 2-D simulations indeed emulate infinitely long fractures in the third dimension. We then subsequently halve the length of the fractures in the direction of the third dimension $D_y$ to mimic more realistic 3-D fractures (bottom plot of Figure B1a). This reduces the magnitudes of the inferred attenuation curves (red, black, and purple curves in Figure B1b). The relative magnitudes of the two peaks as well as the peak frequency remain roughly the same. The loss of amplitude was expected, as the amount of fluid volume in the fracture is reduced with a shortening of the fracture in the third dimension. In the future, simulations on samples featuring more complicated 3-D fracture geometries should be performed to explore pressure diffusion effects in the third dimension in more detail.

**Acknowledgments**
This work has been completed within the Swiss Competence Center on Energy Research-Supply of Electricity with support of the Swiss Commission for Technology and Innovation. The attenuation and modulus dispersion data for this paper are available from https://github.com/rockphysicsUNIL/attenuation_2D.

## References

Barbosa, N., Rubino, J. G., Caspari, E., Guo, J., Gurevich, B., & Holliger, K. (2017). Hybrid modeling of 3D fractured media based on 2D numerical simulations: Aligned fractures case. *SEG Technical Program Expanded Abstracts 2017*, 4200–4204.

Biot, M. A. (1941). General theory for three-dimensional consolidation. *Journal of Applied Physics*, *12*, 155–164.

Biot, M. A. (1962). Mechanics of deformation and acoustic propagation in porous media. *Journal of Applied Physics*, *33*, 1482–1498.

Bonnet, E., Bour, O., Odling, N. E., Davy, P., Main, I., Cowie, P., & Berkowitz, B. (2001). Scaling of fracture systems in geological media. *Reviews of geophysics*, *39*(3), 347–383.

Bour, O., & Davy, P. (1997). Connectivity of random fault networks following a power law fault length distribution. *Water Resources Research*, *33*(7), 1567–1583.

Brajanovski, M., Gurevich, B., & Schoenberg, M. (2005). A model for *P*-wave attenuation and dispersion in a porous medium permeated by aligned fractures. *Geophysical Journal International*, *163*, 372–384.

Caspari, E., Milani, M., Rubino, J. G., Müller, T. M., Quintal, B., & Holliger, K. (2016). Numerical upscaling of frequency-dependent *P*- and *S*-wave moduli in fractured porous media. *Geophysical Prospecting*, *64*, 1166–1179.

Chapman, M. (2003). Frequency-dependent anisotropy due to meso-scale fractures in the presence of equant porosity. *Geophysical Prospecting*, *51*(5), 369–379. https://doi.org/10.1046/j.1365-2478.2003.00384.x

Chapman, M. (2009). Modeling the effect of multiple sets of mesoscale fractures in porous rock on frequency-dependent anisotropy. *Geophysics*, *74*(6), D97–D103.

de Dreuzy, J.-R., Davy, P., & Bour, O. (2001). Hydraulic properties of two-dimensional random fracture networks following a power law length distribution: 1. Effective connectivity. *Water Resources Research*, *37*, 2065–2078.

Galvin, R. J., & Gurevich, B. (2006). Interaction of an elastic wave with a circular crack in a fluid-saturated porous medium. *Applied Physics Letters*, *88*, 61918.

Grechka, V., & Kachanov, M. (2006). Seismic characterization of multiple fracture sets: Does orthotropy suffice? *Geophysics*, *71*(3), D93–D105.

Gurevich, B., Brajanovski, M., Galvin, R. J., Müller, T. M., & Toms-Stewart, J. (2009). *P*-wave dispersion and attenuation in fractured and porous reservoirs—Poroelasticity approach. *Geophysical Prospecting*, *57*(2), 225–237. https://doi.org/10.1111/j.1365-2478.2009.00785.x

Gurevich, B., Zyrianov, V. B., & Lopatnikov, S. L. (1997). Seismic attenuation in finely layered porous rocks: Effects of fluid flow and scattering. *Geophysics*, *62*(1), 319–324.

Hunziker, J., Favino, M., Caspari, E., Quintal, B., Rubino, J. G., Krause, R., & Holliger, K. (2017). Seismic attenuation in realistic fracture networks. In *Proceedings of the 6th Biot Conference on Poromechanics*.

Jänicke, R., Quintal, B., & Steeb, H. (2015). Numerical homogenization of mesoscopic loss in poroelastic media. *European Journal of Mechanics A/Solids*, *49*, 382–395.

Kachanov, M. (1992). Effective elastic properties of cracked solids: Critical review of some basic concepts. *Applied Mechanics Reviews*, *45*(8), 304–335.

Liu, E., & Martinez, A. (2012). *Seismic fracture characterization: Concepts and practical applications*. Houten: European Association of Geoscientists and Engineers.

Liu, E., Hudson, J. A., & Pointer, T. (2000). Equivalent medium representation of fractured rock. *Journal of Geophysical Research*, *105*(B2), 2981–3000. https://doi.org/10.1029/1999JB900306

Masson, Y. J., & Pride, S. R. (2007). Poroelastic finite difference modeling of seismic attenuation and dispersion due to mesoscopic-scale heterogeneity. *Journal of Geophysical Research*, *112*, B03204. https://doi.org/10.1029/2006JB004592

Mavko, G., Mukerji, T., & Dvorkin, J. (2009). *The rock physics handbook* (2nd ed.). Cambridge University Press.

Novikov, M., Caspari, E., Lisitsa, V., Quintal, B., Rubino, J. G., & Holliger, K. (2017). Numerical study of fracture connectivity response in seismic wavefields. *SEG Technical Program Expanded Abstracts 2017*, 3786–3790.

O'Connell, R. J., & Budiansky, B. (1978). Measures of dissipation in viscoelastic media. *Geophysical Research Letters*, *5*, 5–8.

Pevzner, R., Müller, T. M., Galvin, R. J., & Gurevich, B. (2012). Estimation of attenuation from zero-offset VSP data: CO2CRC Otway Project case study. *SEG Technical Program Expanded Abstracts 2012*, 1–6.

Quintal, B., Jänicke, R., Rubino, J. G., Steeb, H., & Holliger, K. (2014). Sensitivity of *S*-wave attenuation to the connectivity of fractures in fluid-saturated rocks. *Geophysics*, *79*, WB15–WB24.

Quintal, B., Steeb, H., Frehner, M., & Schmalholz, M. (2011). Quasi-static finite element modeling of seismic attenuation and dispersion due to wave-induced fluid flow in poroelastic media. *Journal of Geophysical Research*, *116*, B01201. https://doi.org/10.1029/2010JB007475

Renshaw, C. E., & Park, J. C. (1997). Effect of mechanical interactions on the scaling of fracture length and aperture. *Nature*, *386*, 482–484.

Rubino, J. G., Caspari, E., Müller, T. M., & Holliger, K. (2017). Fracture connectivity can reduce the velocity anisotropy of seismic waves. *Geophysical Journal International*, *210*, 223–227.

Rubino, J. G., Guarracino, L., Müller, T. M., & Holliger, K. (2013). Do seismic waves sense fracture connectivity? *Geophysical Research Letters*, *40*, 692–696. https://doi.org/10.1002/grl.50127

Rubino, J. G., Ravazzoli, C. L., & Santos, J. E. (2009). Equivalent viscoelastic solids for heterogeneous fluid-saturated porous rocks. *Geophysics*, *74*, N1–N13.

Rubino, J. G., Müller, T. M., Guarracino, L., Milani, M., & Holliger, K. (2014). Seismoacoustic signatures of fracture connectivity. *Journal of Geophysical Research: Solid Earth*, *119*, 2252–2271. https://doi.org/10.1002/2013JB010567

Schoenberg, M., & Sayers, C. M. (1995). Seismic anisotropy of fractured rock. *Geophysics*, *60*(1), 204–211.

Solazzi, S. G., Rubino, J. G., Müller, T. M., Milani, M., Guarracino, L., & Holliger, K. (2016). An energy-based approach to estimate seismic attenuation due to wave-induced fluid flow in heterogeneous poroelastic media. *Geophysical Journal International*, *207*, 823–832.

Vermilye, J. M., & Scholz, C. H. (1995). Relation between vein length and aperture. *Journal of Structural Geology*, *17*, 423–434.

Vinci, C, Renner, J, & Steeb, H (2014). On attenuation of seismic waves associated with flow in fractures. *Geophysical Research Letters*, *41*, 7515–7523. https://doi.org/10.1002/2014GL061634

White, J. E., Mikhaylova, N. G., & Lyakhovitskiy, F. M. (1975). Low-frequency seismic waves in fluid-saturated layered rocks. *Izvestiya, Academy of Sciences, USSR. Physics of the Solid Earth*, *11*, 654–659.

Wu, R.-S. (1985). Multiple scattering and energy transfer of seismic waves - separation of scattering effect from intrinsic attenuation - I. Theoretical modelling. *Geophysical Journal of the Royal Astronomical Society*, *82*, 57–80.